Advanced Powder Materials 3 (2024) 100163

Contents lists available at ScienceDirect

Advanced Powder Materials

journal homepage: www.keaipublishing.com/en/journals/advanced-powder-materials

Oxidation behavior of amorphous and nanocrystalline SiBCN ceramics – Kinetic consideration and microstructure

Zibo Niu [a,b], Daxin Li [a,b,*], Dechang Jia [a,b,c,**], Zhihua Yang [a,b,c,d], Kunpeng Lin [a,b], Ralf Riedel [e], Paolo Colombo [f,g], Yu Zhou [a,b,c,h]

[a] Institute for Advanced Ceramics, School of Materials Science and Engineering, Harbin Institute of Technology, Harbin 150080, China
[b] Key Laboratory of Advanced Structural-Function Integrated Materials and Green Manufacturing Technology, Ministry of Industry and Information Technology, Harbin 150080, China
[c] State Key Laboratory of Advanced Welding and Joining, Harbin Institute of Technology, Harbin, 150080, China
[d] Chongqing Research Institute, Harbin Institute of Technology, Chongqing 401135, China
[e] Institute of Materials Science, Darmstadt University of Technology, Otto-Berndt-Str. 3, 64287, Darmstadt, Germany
[f] Department of Industrial Engineering, University of Padova, Via Marzolo, 9, Padova, Italy
[g] Department of Materials Science and Engineering, The Pennsylvania State University, University Park, PA 16802, United States
[h] School of Materials Science and Engineering, Harbin Institute of Technology (Shenzhen), Shenzhen 518055, China

ARTICLE INFO

Keywords:
SiBCN ceramics
Amorphous
Crystallization
Oxidation
Kinetics analysis

ABSTRACT

In this study, the structural evolution of SiBCN ceramics during crystallization and its effects on oxidation behavior involving different atomic units or formed phases in amorphous or crystalline SiBCN ceramics were analyzed. The amorphous structure has exceptionally high oxidation activity but presents much better oxidation resistance due to its synchronous oxidation of atomic units and homogeneous composition in the generated oxide layer. However, the oxidation resistance of SiBCN ceramic will degrade during the continual crystallization process, especially for the formation of the nanocapsule-like structure, due to heterogeneous oxidation caused by the phase separation. Besides, the activation energy and rate-controlling mechanism of the atomic units and phases in SiBCN ceramics were obtained. The BNC_x ($E_a = 145$ kJ/mol) and $SiC_{(2-x)}$ ($E_a = 364$ kJ/mol) atomic units in amorphous SiBCN structure can be oxidized at relatively lower temperatures with much lower activation energy than the corresponding BN(C) ($E_a = 209$ kJ/mol) and SiC ($E_a = 533$ kJ/mol) phases in crystalline structure, and the synchronous oxidation of the $SiC_{(2-x)}$ and BNC_x units above 750 °C changes the oxidation activation energy of BNC_x ($E_a = 332$ kJ/mol) to that similar to $SiC_{(2-x)}$. The heterogeneous oxide layer formed from the nanocapsule-like structure will decrease the activation energy SiC ($E_a = 445$ kJ/mol) and t-BN ($E_a = 198$ kJ/mol).

1. Introduction

Due to their combination of extraordinary high-temperature stability (up to 2000 °C) [1–3] and oxidation resistance (up to 1800 °C) [4–6] with the stability of useful functional properties up to these very high temperatures [7–9], amorphous silicoboron carbonitride (SiBCN) ceramics were developed as structural-functional material for high-temperature harsh environments [8–10]. Despite the uniform and disordered atom distribution on the nanoscale, amorphous SiBCN ceramics also have near-ordered structure and are composed of silicon atom units bonded by sp^3 hybridization related with B–C–N atomic units bonded by sp^2 hybridization [11,12]. Therefore, the temperature stability and oxidation resistance of SiBCN material strongly depend on the strong three-dimensional amorphous network covalent bonding structure composed of the microscopic atom units.

However, although extensive investigations have been carried out regarding the oxidation behavior and kinetics of SiBCN ceramics, the existing research mainly focuses on the oxide layer growth such as oxide layer structure, growth kinetic law and oxygen diffusion mechanism [4,5,13–16], and no theory to systematically explain the microscopic mechanism and kinetics of oxidation of amorphous SiBCN ceramics involving different atoms units has been developed yet. In fact, the characterization

* Corresponding author. Institute for Advanced Ceramics, School of Materials Science and Engineering, Harbin Institute of Technology, Harbin 150080, China.
** Corresponding author. Institute for Advanced Ceramics, School of Materials Science and Engineering, Harbin Institute of Technology, Harbin 150080, China.
E-mail addresses: lidaxin@hit.edu.cn (D. Li), dcjia@hit.edu.cn (D. Jia).

https://doi.org/10.1016/j.apmate.2023.100163
Received 27 July 2023; Received in revised form 3 September 2023; Accepted 17 September 2023
Available online 28 September 2023

of oxidation of the different atomic units in amorphous SiBCN ceramics is still a challenge. For one thing, the atomic units in amorphous ceramics lie between the world of single atoms and molecules and the macroscopic world, presenting different oxidation mechanisms and kinetics from traditional polycrystalline ceramics [17,18]. For another, the two kinds of atomic units with various compositions and chemistry have different oxidation activities and kinetic laws, and interacting with each other during the oxidation process. Therefore, the similar characterization of mass variation and oxide layer growth to other crystalline ceramics cannot describe the oxidation mechanism of amorphous SiBCN ceramics involving its near-ordered structure.

Besides, the amorphous SiBCN ceramics will inevitably crystallize to nanostructure during long-term high-temperature applications [19,20], while the effects of amorphous-to-crystalline transformation on the oxidation behaviors of SiBCN ceramics were rarely reported. Therefore, oxidation experiments up to 1500 °C of amorphous and crystallized SiBCN monolith were carried out prior to our studies. Amorphous SiBCN ceramics present substantially different oxidation behavior and greater oxidation performance than crystallized SiBCN ceramics. Interestingly, the oxidation phenomenon can be well explained by the conclusion of this paper. Detailed experimental results and analysis can be taken from Section 4 in the supplementary material. Therefore, it is necessary to systematically study the effects of the amorphous-to-crystalline evolution on the oxidation behavior and kinetics law of SiBCN ceramics.

This paper, therefore, aims at determining the oxidation behavior and kinetic law of amorphous SiBCN ceramics involving different near-ordered structures and uncovering the influence of amorphous-to-crystalline evolution on the oxidation of SiBCN ceramics. In this study, amorphous SiBCN ceramic synthesized by mechanical alloying (MA) was selected due to its relatively simple near-ordered structure [21,22]. The MA-SiBCN ceramic was refined to the nanoscale to amplify the signal of oxidation rate and then was crystallized at different temperatures to explore the impacts of the structural evolution during crystallization on the oxidation of SiBCN ceramics. The structural evolution of SiBCN ceramics during crystallization was investigated and the influences of structural evolution on the oxidation behavior of SiBCN ceramics were obtained by non-isothermal oxidation experiment. Besides, the oxidation behavior and interaction of different atomic units or formed phases in amorphous or crystalline SiBCN ceramics and their effect on the generated oxide layer were analyzed. Finally, by kinetic calculation, the activation energy and rate-controlling mechanism of the oxidation of the atomic units and phases in the SiBCN ceramics at different temperatures was determined, which perfectly corresponds to the experimentally observed oxidation behaviors.

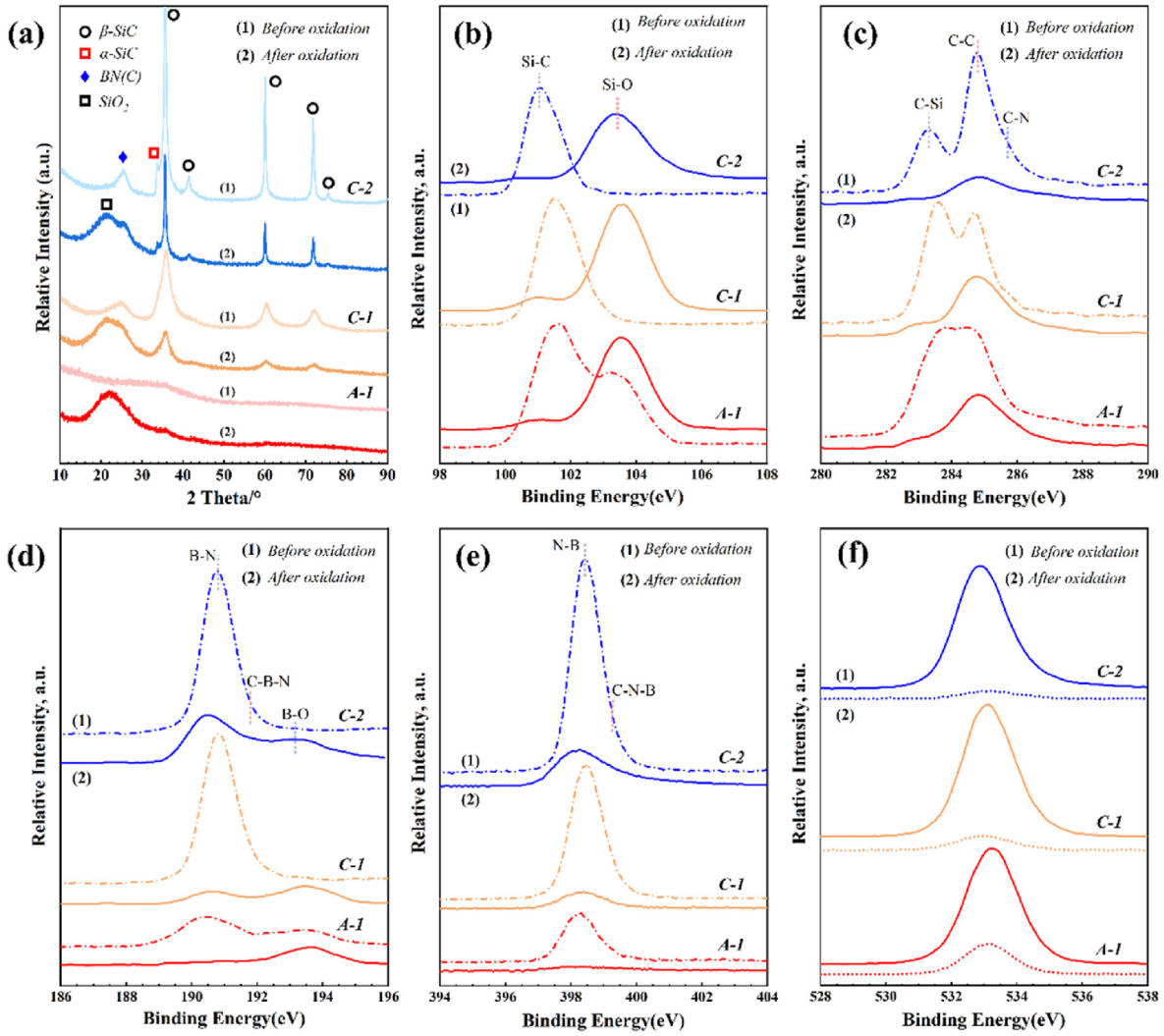

Fig. 1. XRD (a) and XPS (b–f) spectra of different SiBCN ceramics before and after oxidation: (b) Si; (c) C; (d) B; (e) N; (f) O.

2. Results and discussion

2.1. Structural evolution and phase separation of SiBCN ceramics during crystallization

2.1.1. Structural evolution in SiBCN ceramics during crystallization

Fig. 1(a) shows the XRD patterns of amorphous and crystallized SiBCN ceramics before and after non-isothermal oxidation. Accordingly, Sample A-1 presents an amorphous structure without any diffraction peak in the XRD pattern while crystalline phases of β/α-SiC and turbostratic BN(C) appear in annealed C-1 and C-2 samples. Note that the BN(C) phase is composed of mutually doped and stacked turbostratic carbon (t-C) and turbostratic boron nitride (t-BN) [19]. With increasing annealing temperature, the crystalline phases, especially β-SiC in Sample C-2 significantly grow as compared to that in Sample C-1. For example, according to the Scherrer formula (see **Eq. (S1)**), the average grain size of the β-SiC phase in Sample C-2 is around 16.3 nm and much higher than that of Sample C-1 (3.5 nm) indicating structural evolution of muti-phase structure at higher annealing temperatures.

Fig. 2 (a-d) shows the microstructure and electron diffraction patterns of A-1 (a-c) and C-1 samples (d). As shown in Fig. 2(a-c), Sample A-1 does not show any obvious lattice pattern in the high-resolution TEM image (see Fig. 2(b)) and any diffraction ring and diffraction spots in the corresponding selected area electron diffraction (SAED) pattern, further indicating the amorphous structure of Sample A-1. As shown in Fig. 2(d), a large number of SiC and BN(C) microcrystallines with a size of 2–5 nm (approaching the calculation value from the XRD pattern) precipitate from the amorphous structure. Due to the lower crystallization temperature, SiC microcrystalline has a certain degree of lattice distortion presenting (111) crystal plane with a larger distance (2.59 Å) and a certain degree of deviation and some adjacent SiC grains have a similar orientation relationship to SiC twins to reduce grain-boundary energy by coherent state: the (111) crystal plane of adjacent grains is symmetrical with each other with the crystal plane angle of $\theta = 70.5^{\circ}$ and (11–1) crystal plane as twin boundary Besides, an BN(C) is precipitated preferentially on the surface to form a BN(C) phase-rich edge with a thickness of about 2–3 nm.

Fig. 2(e–f) and Fig. S1 show the microstructure and electron diffraction patterns of Sample C-2. As shown in Fig. 2(e), various SiC grains (dark area) with a grain size of about 20–50 nm are encapsulated by turbostratic BN(C) phase, presenting a nanocapsule-like structure in Sample C-2, corresponding to the diffraction pattern in Fig. S1(a). As shown in Fig. S1(b), BN(C) phase in the nanocapsule-like structure has a loosely stacked turbostratic with a (002) crystal plane spacing of about 3.41 Å, while the SiC grain presents an almost perfect crystal structure without obvious lattice distortion and defects. Compared with Sample C-1, the interplanar spacings of SiC and BN(C) phases, especially the BN(C) phase, in Sample C-2 are closer to the theoretical value indicating further

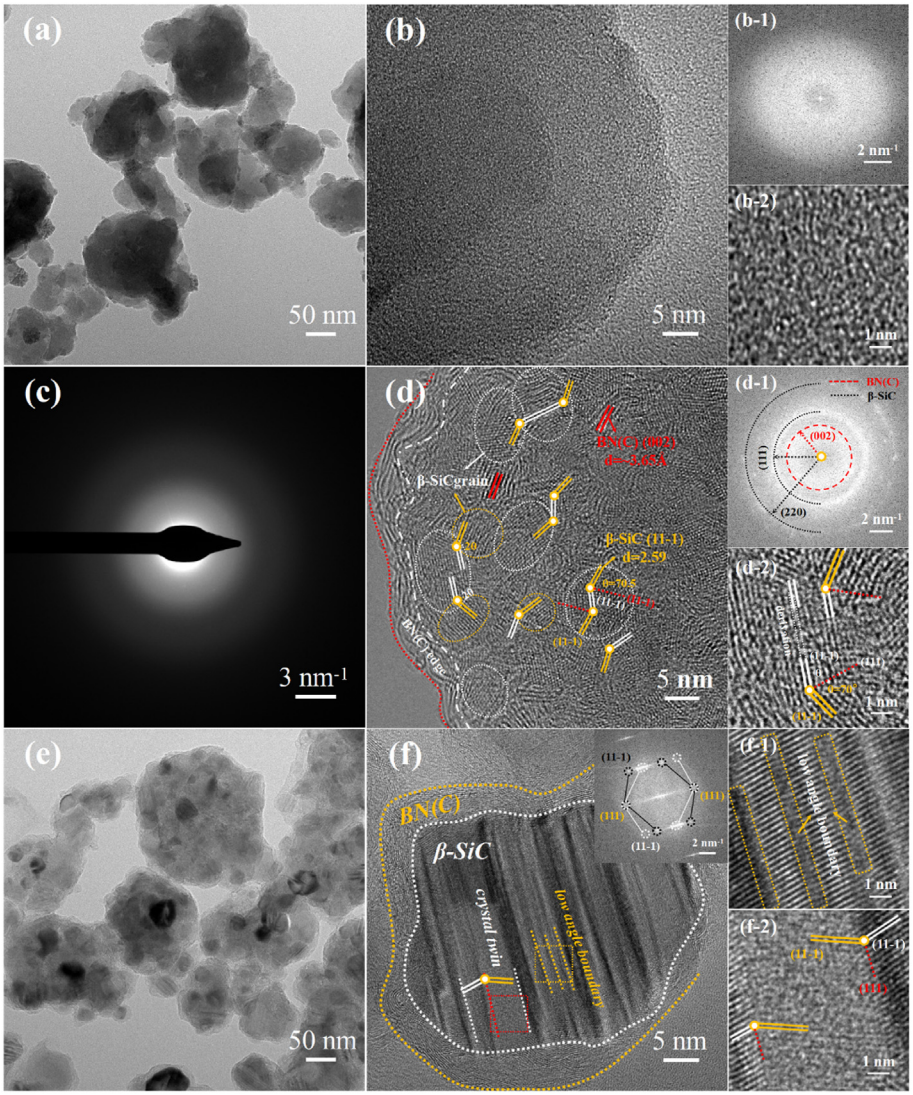

Fig. 2. TEM images of the microstructure of Sample A-1 (a–c), Sample C-1 (d), and Sample C-2 (e–f): the yellow or white double lines in (d) mark the (111) crystal plane of β-SiC and symmetrical orientation relationship between adjacent grains; (d-1) and (d-2) are Fourier transform diagram and enlarged image of (d); the twin boundaries in (f) and the low angle boundary in abnormally grown SiC grain are marked by red dotted line and yellow dotted line respectively, causing the axially symmetrical diffraction patterns and deformation of some diffraction spots in its Fourier transform diagram (upper illustration); (f-1) and (f-2) are the enlarged images of yellow and red squares in (f) respectively, showing the low angle boundary and twin structure in abnormally grown SiC grain.

ordering of each phase at the higher crystallization temperature. Ordering or graphitization of the BN(C) phase is also proved by the Raman spectra of the SiBCN ceramics in Fig. S2. As shown in Fig. S2, the free carbon formed by phase separation, mainly the t-C in BN(C) phase, in the crystallized C-1 and C-2 samples causes the obvious G peak at 1580 cm^{-1} and D peak at 1340 cm^{-1} in the Raman spectrum, corresponding to in-plane sp^2 stretching vibration and defects in the sp^2-hybridized lattice [23]. Through the exponential curve regression model, graphitization parameters (g) of the BN(C) phase can be calculated from the ratio of the G peak intensity (I_G) to the D peak intensity (I_D) (I_D/I_G) by Eq. (S2) [24, 25]. Accordingly, the graphitization parameter (g) of the BN(C) phase in Sample C-2 (21%) is significantly higher than that in Sample C-1 (6%) indicating a much higher graphitization degree of the BN(C) phase in Sample C-2.

It should be noted that some abnormally grown SiC grain (>50 nm) exist in the nanocapsule-like structure However, abnormally grown SiC grain is not a complete single crystal and can be subdivided by many parallel twin boundaries and small angle boundaries (see Fig. 2(f)) with a certain interval. The adjacent SiC crystallites in the microcrystalline structure of Sample C-1 evolve into the abnormally grown SiC grain by twisting and merging, so the abnormally grown SiC grain shows the inheritance from the microstructure of Sample C-1. Specifically, during mutual annexation of SiC crystallites, the orientation relationship between adjacent SiC crystallites in the microcrystalline structure promotes the formation of twin structures in SiC nanocrystals. The lattice distortion in SiC microcrystalline and the orientation deviation between the adjacent SiC crystallites cause the low-angle grain boundaries in the larger SiC grain.

2.1.2. *Phase separation during crystallization and effect on oxidation activities of SiBCN ceramics*

Fig. 1 (b-f) shows the XPS results of the SiBCN ceramics before and after oxidation and the deconvolution of the XPS peaks of different elements in amorphous and crystalline SiBCN ceramics is displayed in Fig. S3 and Fig. S4. Quantification of the local bonding environment of the respective elements as calculated from the deconvolution results is listed in Table 1, which reflects the change in surface/oxidation activity and phase separation during crystallization.

2.1.2.1. Phase separation in the SiBCN ceramics during crystallization. According to the XPS peak deconvolution of Si, B, and N elements in Fig. S3 and Fig. S4, the Si, B and N atoms in the amorphous Sample A-1 have a chemical environment similar to that of the BN(C) and SiC phases in the nanocrystalline structures of the C-1 and C-2 samples, due to the short-range order structure of sp^3 hybridized $SiC_{(2-x)}$ ($x < 1$) and sp^2 hybridized BNC_x in amorphous MA-SiBCN ceramics. The existence of sp^2 hybridized BNC_x units in the amorphous structure is also reflected in the Raman spectrum in Fig. S1. Although the atoms in the BNC_x units are bonded by sp^2 hybridization, there is no complete sp^2 hybridized atom ring with more than a certain scale in the BNC_x unit due to unsaturated and distorted bonding, according to obvious D peak but no G peak in Raman spectrum. Despite a similar chemical environment of Si, B, and N elements, the change in bonding environment of C element in the SiBCN ceramics reflects the phase separation process during crystallization. As shown in Fig. S3(c), the bonding environment of C element in the SiBCN ceramics is mainly composed of C–Si and C–C bonds except for a small number of C–N bonds. With the transformation from amorphous to nanocrystalline structure, the peaks of C–C and C–Si bonds are gradually separated, reflecting the transition from a homogeneous phase to a multiphase microstructure. The C–C and Si–C bonds in the amorphous structure of Sample A-1 are mainly present in BNC_x and $SiC_{(2-x)}$ units, respectively. Due to the excess of C atoms in the $SiC_{(2-x)}$ units ($x < 1$), the C atoms bond with both Si and other C atoms (Si–C–C), resulting in an overlap of peaks of Si–C and C–C bonds. With the phase separation and precipitation of SiC and BN(C) phases during crystallization, the excess carbon precipitates from the $SiC_{(2-x)}$ units to form free carbon. The interaction between BN(C) and SiC only exists at the interface, so that the C atoms bonded to Si and C atoms (Si–C–C) are significantly reduced and the amount of free carbon significantly increases, resulting in a separation of the peaks related to Si–C and C–C bonds. Moreover, the XPS peak intensity of B and N elements also reflects the evolution of multi-phase structure. As shown in Fig. 1(d-e), with the amorphous-to-crystalline transformation, B and N elements are enriched on the surface with an increase in peak intensity, due to the BN(C)-rich edge in Sample C-1 and a nanocapsule-like structure in the Sample C-2. In Fig. 3, the elemental distribution in A-1 and C-2 samples is compared by HAADF images and EDS mapping. For the C-2 samples, the bright particles in the HAADF image (see Figs. 3(b-1)) show the distribution of SiC grains. The Si-rich region is surrounded by the N-rich region (see Figs. 3(b-2)) in the nanocapsule-like structure, leading to the enhanced peak intensity of B and N elements.

Table 1
Quantification of the local bonding environments of different SiBCN ceramics based on deconvoluted XPS spectra.

Valence bond	A-1		C-1		C-2	
	BE (eV)	Content (%)	BE (eV)	Content (%)	BE (eV)	Content (%)
Si–C	101.5	60.0	101.5	84.6	101.1	88.4
Si–O	103.4	40.0	102.5	15.4	101.9	11.6
B–N	190.4	61.6	190.8	94.5	190.8	87.9
C–B–N	192.1	12.8	191.9	5.5	191.4	12.1
B–O	193.5	25.6	–	–	–	–
C–Si	283.5	45.9	283.6	52.4	283.3	29.2
C–C	284.7	42.1	284.7	39.0	284.8	53.4
C–N	286.1	12.0	285.8	8.6	285.7	17.4
N–B (sp^2)	398.3	80.6	190.8	94.5	190.8	87.9
C–N–B	399.6	13.3	191.9	5.5	191.4	12.1
N–O	402.4	6.0	–	–	–	–

2.1.2.2. Effect of crystallization on oxidation activity of SiBCN ceramics. As shown in Fig. 1(f), the peak intensity of O element on the surface of the amorphous Sample A-1 is significantly higher than that of the crystallized C-1 and C-2 samples. Besides, Sample C-2 with the highest crystallization degree has the lowest oxygen content on the surface. The O peaks of all SiBCN ceramics have good symmetry, indicating that the valence bond states of all the oxygen atoms are similar. As shown in Fig. S3(b), compared with C-1 and C-2 samples, the chemical state of Si element in amorphous Sample A-1 contains a large number of Si–O bonds (40.0%) in addition to Si–C bonds. Besides, as shown in Fig. S3(d) the local bonding environment of B in Sample A-1 contains a large number of B–O bonds (25.6%) in addition to B–N (61.6%) and C–B–N (12.8%) bonds. Therefore, Si and B of Sample A-1 react with oxygen in the air even at room temperature to form a large number of B–O and Si–O bonds at the surface. Although the peaks of Si–O and B–O bonds cannot be identified in the XPS spectra of Si and B elements in the C-1 and C-2 samples, it is worth noting that the XPS peaks of Si–C bond in the C-1 and C-2 samples have a certain degree of asymmetry on the high binding energy side. According to their weak XPS peaks of O, the electromagnetic interaction between the unsaturated Si atoms on the surface of the SiC grains and the chemisorbed oxygen increases the binding energy of Si, resulting in asymmetry on the high binding energy side. As shown in Fig. S3(b-3), Sample C-2 with a higher crystallization degree has a smaller asymmetric area (11.6%) than that of Sample C-1 (15.4%), because after crystallization the atoms in nanocrystalline ceramics tend to coordination saturation and is hard to bond with oxygen at room temperature.

As shown in Fig. S4(e), N element forms N–B and C–N–B bonds in all SiBCN ceramics. However, the amorphous Sample A-1 also shows the presence of 6% and 19% of N–O bonds before and after high-temperature oxidation, respectively. In contrast, for the crystalline C-1 and C-2

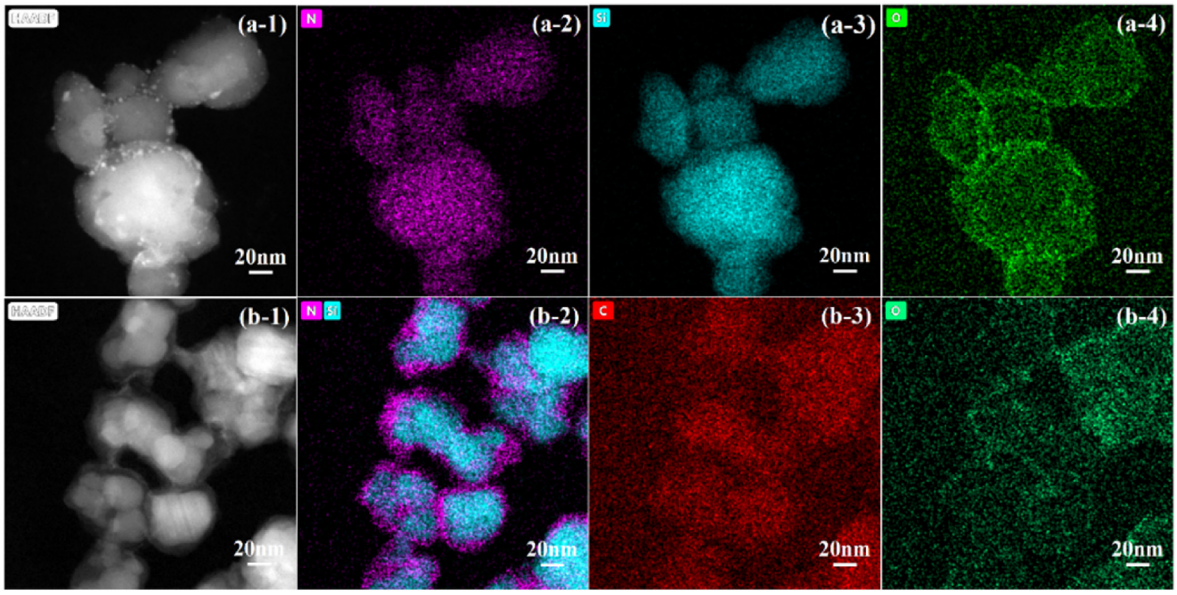

Fig. 3. HAADF images and EDS mappings of the A-1 (a) and C-2 samples (b).

samples, N–O bonds do not appear even after high-temperature oxidation. Like the formation of B–O and Si–O bonds, the N atoms on the surface of the amorphous Sample A-1 can bond with O atoms to form N–O bonds due to the unsaturated coordination in the amorphous structure. However, the N atoms in C-1 and C-2 samples are mainly distributed in BN(C) phase and bond with B atoms and a small number of doped C atoms by sp^2 hybridization, so the N atoms with saturated electron shell are hard to bond with oxygen at room temperature and the N–O bond formed during high-temperature oxidation is also quickly converted into NO or NO_2. As shown in Figs. 3(a-4), compared with crystalline Sample C-2, more oxygen content is enriched on the surface of the amorphous Sample A-1, especially on the fine particles with a size of around 1–3 nm located on the surface. Therefore, the amorphous Sample A-1 is severely oxidized even at room temperature to form fine oxide particles containing Si–O, B–O and N–O bonds on their surface which is rare for the strong covalent bonding structure, while crystallization leads to a decrease in oxidation activity, due to the disappearance of vacancies and dangling bonds in three-dimensional amorphous network covalent bonding structure. It should be noted that the oxygen content sample of A-1 (5.1 wt%) is only slightly higher than that of C-1 (3.8 wt%) and C-2 samples (3.4 wt%) and the difference in oxygen content between amorphous and crystalline structures is not as obvious as the XPS results, because the XPS results only reflect element and the valence bond composition on the surface with characterization depth of only 3–5 nm. Therefore, the limited difference in oxygen content is derived from the oxidation of the active site rather than the amorphous structure, so the influence of the difference in oxygen content on oxidation behavior is very limited.

2.2. Oxidation behavior of SiBCN ceramics containing different atomics units or phases

Fig. 4(a–c) shows the thermogravimetric (TG), derivative thermogravimetric (DTG), differential scanning calorimetry (DSC) and mass spectra (MS) of the gas product during non-isothermal oxidation of amorphous Sample A-1, Sample C-1 with microcrystalline microstructure and Sample C-2 with nanocapsule-like microstructure. Besides, the mass change, mass change rate and heat effect of A-1, C-1 and C-2 samples are compared in Fig. 4(d-f). As shown in Fig. 4(a-c), the oxidation process of the three kinds of SiBCN ceramic can be subdivided into three stages: in the low-temperature range (RT∼550), the SiBCN ceramics display little change in mass and no heat effect. In the middle-temperature range (550–1000/1200 °C), all SiBCN ceramics present a mass change in TG curves, exothermic peaks in the DSC curves and mass spectra of different gas products, indicating significant oxidation. Fig. S5 shows the change of standard Gibbs free energy of different oxidation reactions with temperature. Each reaction (Eqs. (1)–(6)) conforms to thermodynamic conditions in the whole temperature range (RT-1500 °C) and the reaction rate is controlled by kinetic conditions [26], so the mass change and thermal effect in the middle-temperature stage are the comprehensive results of the different reaction processes. The oxidation of carbon (Eqs. (1-2)) and the volatilization of B_2O_3 (Eq. (7)) lead to weight loss, and the oxidation of BN (Eqs. (3-4)) and SiC (Eqs. (5-6)) lead to weight gain. Note that SiC, BN and C in Eqs. (1)–(6) do not represent different phases, but different bonding environments of the atoms. Therefore, it is still impossible to distinguish between the oxidation of different atomic units and phases in the SiBCN ceramics at different temperatures just by the change of mass. Fortunately, due to the different starting temperatures of the individual reactions and their different gas products, combined with TG and DSC curves, the mass spectra of the different gas products can reflect oxidation rates of different reactions associated with the different atomic units or phases in the SiBCN ceramics. However, after the middle-temperature range, the mass increases slowly and the peak intensities of the mass spectra maintain a relatively low level in the high-temperature range (>1000/1200 °C), indicating a change in the rate-controlling steps of oxidation in the high-temperature stage. The oxidation behaviors of the SiBCN ceramics in each temperature range have been exemplarily analyzed with Sample A-1 in Section 2.2.1 below.

2.2.1. Oxidation behavior of amorphous SiBCN ceramics with atomic units of $SiC_{(2-x)}$ and BNC_x

As shown in Fig. 4(a), at RT-250 °C, Sample A-1 yields a slight weight loss (0.2%), accompanied by the appearance of an MS peak of $m/z = 18$ (H_2O) and an endothermic DSC peak, indicating no chemical reaction, except for volatilization of absorbed moisture. Between 250 and 550 °C, Sample A-1 presents a slight mass increase (0.5%) and a weak exothermic DSC peak and the MS peaks of $m/z = 28$ (CO/N_2), 30 (NO), 44 (CO_2) in the mass spectra also increase gradually. This result is discussed in terms that due to the extremely high oxidation activity of amorphous structure oxidation reactions already start even at such low temperatures to form Si–O and B–O related oxide phases at the surface with the release of C–O and N–O related gaseous products.

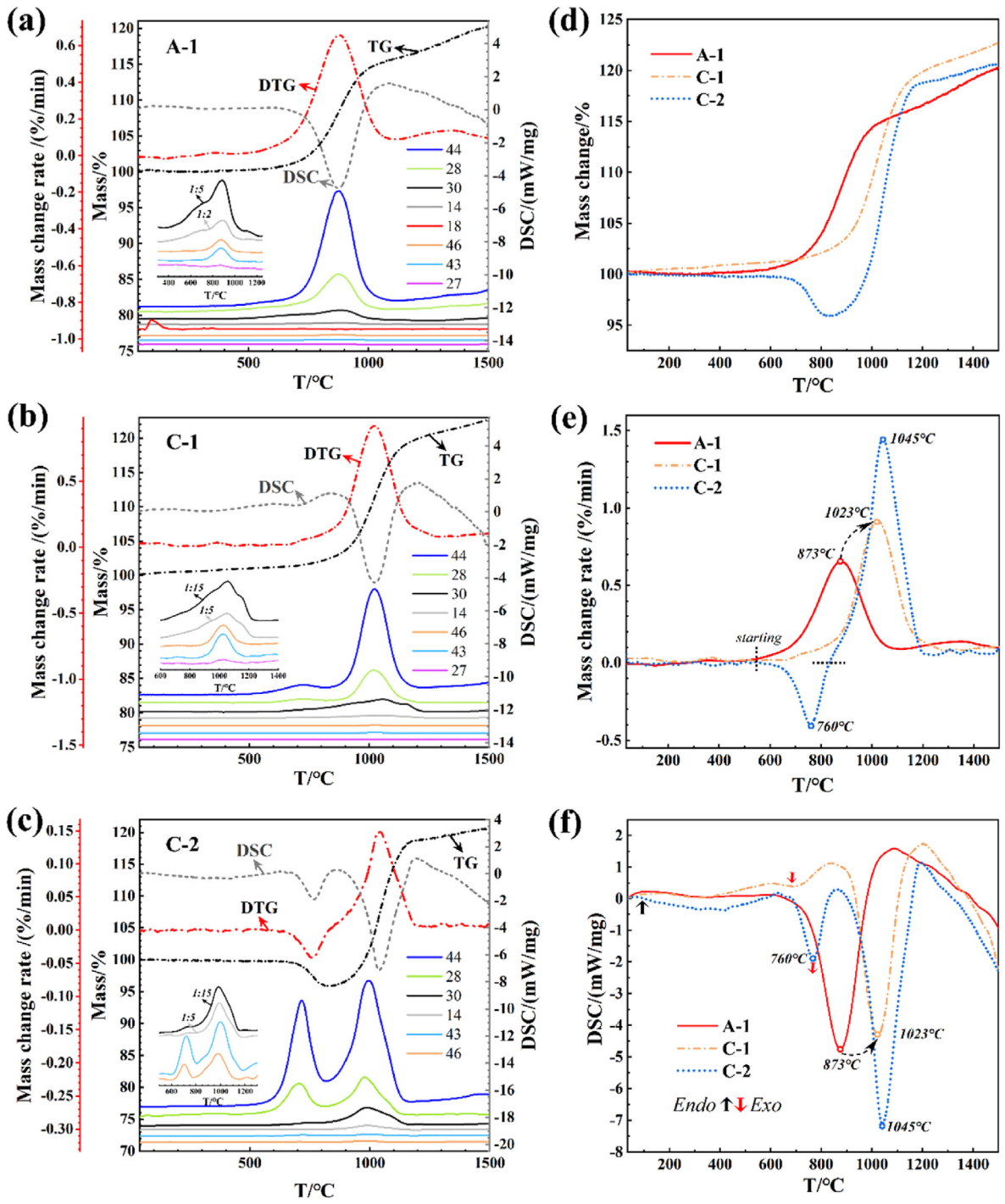

Fig. 4. TG, DTG, and DSC curves and MS spectra of gas product evolved during non-isothermal oxidation of A-1 (a), C-1 (b), and C-2 (c) samples; (d)–(f): mass change, mass change rate, and DSC of A-1, C-1, and C-2 samples for comparison.

In the middle-temperature range (550–1000 °C), the mass of Sample A-1 begins to increase significantly (15 wt%) and the DTG and DSC curves show a single weight gain peak and an exothermic peak, respectively with a similar peak shape, reflecting the overall oxidation rate of the amorphous phase. Besides, obvious peaks appear in the mass spectra of $m/z = 44$, 28 and 30, corresponding to the gaseous oxidation products of CO_2, CO/N_2, except for the relatively weak peaks of $m/z = 14$, 27, 43, and 46 caused by the slight release of N_2, BO, BO_2, and NO_2, respectively. Obviously, the $SiC_{(2-x)}$ units are oxidized to form SiO_2 releasing CO and CO_2 while the BNC_x units are oxidized to B_2O_3 releasing CO_2, CO, N_2, NO and NO_2. Note that the coincidence degree between the mass spectra of $m/z = 28$ and $m/z = 44$ in the middle-temperature range after normalization is extremely high (see Fig. S6), indicating that the peak intensity of $m/z = 28$ mainly reflects the presence of CO, due to a relatively lower concentration of N_2. Besides, after normalization, the MS peak intensity of the $m/z = 28$ (N_2) is slightly higher than that of $m/z = 44$ (CO_2), especially at lower temperatures (<750 °C), which reflects the presence of a small amount of N_2, mainly due to the relatively low yield of CO at lower temperatures. Therefore, since the concentrations of CO and CO_2 should be proportional, the peak intensity of $m/z = 44$ is a measure of the oxidation rate of C in the amorphous Sample A-1. In addition, after normalization, the MS peak of $m/z = 14$ almost coincides with that of $m/$

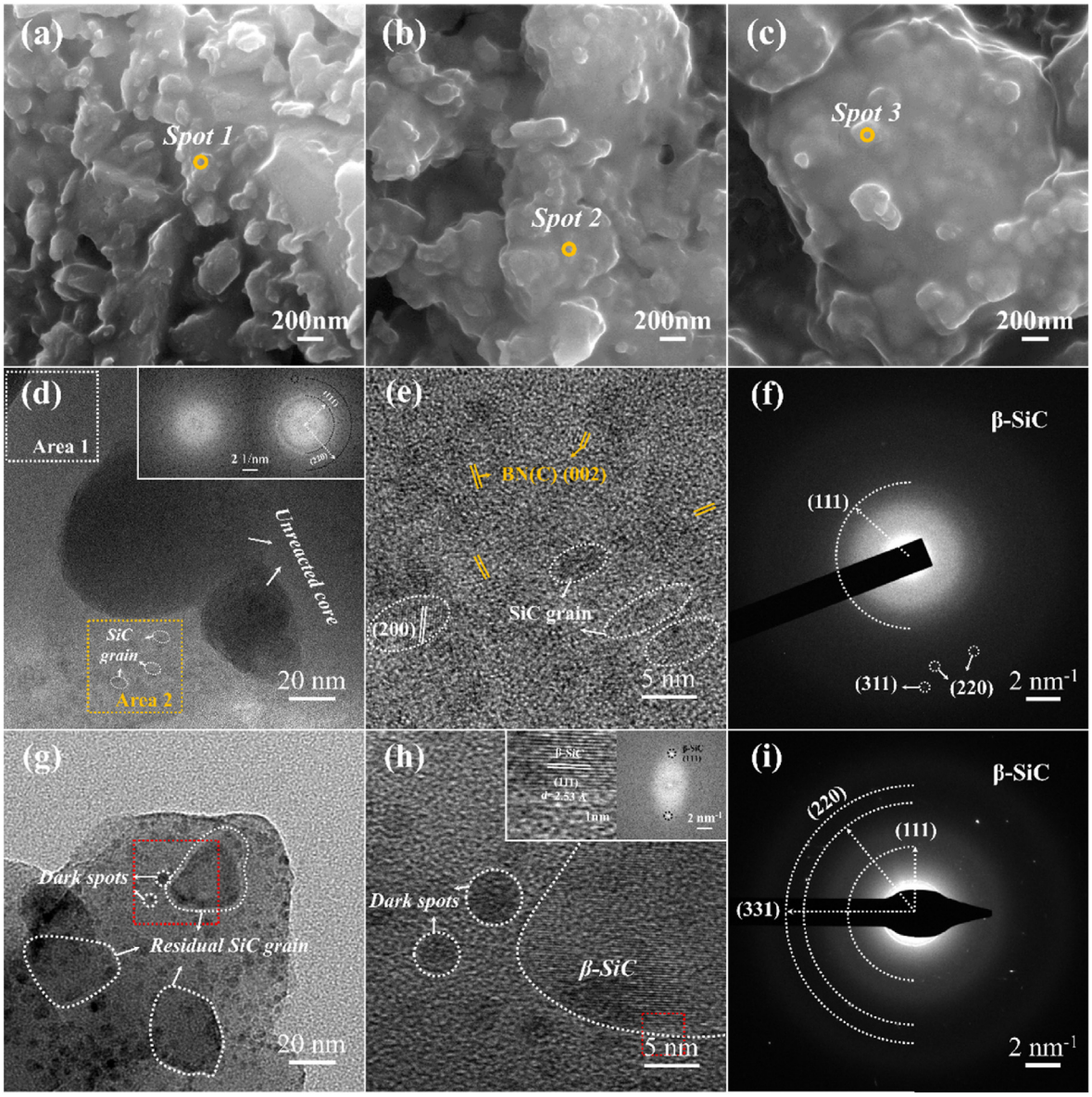

Fig. 5. Internal structure of the oxidized A-1 (a), C-1 (b), and C-2 (c) samples and microstructure of the oxidized crystalline C-1 (d–f) and C-2 (g–i) samples with their electron diffraction patterns: upper illustration of (d) are Fourier transform diagram of Area 1 (left) and Area 2 (right), respectively; (e) is the enlarged image of Area 2 in (d); (h) is the enlarged image of red square in (g); the upper illustrations of (h) are the enlarged image of red square in (h) and its Fourier transform diagram.

$z = 30$, indicating that the oxidation rate of the BNC_x atomic unit can be reflected by the peak intensity of the MS peak of $m/z = 30$ or 14. During the whole non-isothermal oxidation process, no MS peaks of m/z = 68–70 (B_2O_3) are found. Nevertheless, this does not mean, that there is no volatilization of B_2O_3 since volatilized B_2O_3 will condense before reaching the collector and, thus cannot be detected. However, as shown in Fig. 4(a), the MS peaks related to BO_2 ($m/z = 43$) and BO ($m/z = 27$) appear in the intense exothermic stage (700–1000 °C), indicating that volatile boron oxides can be formed at high temperatures and decomposed to BO_2 and BO molecules due to the severe heat release.

$$2C(s) + O_2(g) \rightarrow 2CO(g)\ \Delta G_1^{\Theta} = -228800 - 171.54T \quad (1)$$

$$2C(s) + 2O_2(g) \rightarrow 2CO_2(g)\ \Delta G_2^{\Theta} = -790700 - 1.08T \quad (2)$$

$$BN(s) + \frac{3}{4}O_2(g) \rightarrow \frac{1}{2}B_2O_3(l) + \frac{1}{2}N_2\ \Delta G_2^{\Theta} = -360431 + 13.6T \quad (3a)$$

$$BN(s) + \frac{5}{4}O_2(g) \rightarrow \frac{1}{2}B_2O_3(s) + NO(g)\ \Delta G_3^{\Theta} = -270015 + 0.92T \quad (3b)$$

$$BN(s) + \frac{7}{4}O_2(g) \rightarrow \frac{1}{2}B_2O_3(s) + NO_2(g)\ \ \Delta G_4^{\Theta} = -327331 + 74.48T \quad (4)$$

$$SiC(s) + \frac{3}{2}O_2(g) \rightarrow SiO_2(s) + CO(g)\ \ \Delta G_5^{\Theta} = -955396 + 80.46T \quad (5)$$

$$SiC(s) + \frac{5}{2}O_2(g) \rightarrow SiO_2(s) + CO_2(g)\ \Delta G_6^{\Theta} = -1236346 + 165.69T \quad (6)$$

$$B_2O_3(l) \rightarrow B_2O_3(g) \quad (7)$$

According to the above analysis, the MS peak intensity of $m/z = 30$ reflects the change of the oxidation rate of BNC_x with temperature, while oxidation of both BNC_x and $SiC_{(2-x)}$ contributes to the peak intensity of $m/z = 44$. However, in the middle-temperature range (550–1000 °C), the mass spectra of $m/z = 30$ and 44 show an obvious deflection at 750 °C,

indicating a change in the oxidation mechanisms of both $SiC_{(2-x)}$ and BNC_x between the lower temperature (550–750 °C) and higher temperature regimes (750–1000 °C). In the lower temperature regime, the MS peak of $m/z = 30$ (NO) has a certain peak intensity, indicating that BNC_x begins to be oxidized, while the relatively weak peak intensity of $m/z = 44$ (CO_2) attributed to the oxidation of C atoms in BNC_x increases slowly. In addition, according to the normalized MS peaks of $m/z = 28$ and 44 at lower temperatures (250–750 °C), the presence of a small amount of N_2 also reflects the oxidation of BNC_x in the lower temperature regime. However, in the higher temperature regime, the MS peak of $m/z = 44$ begins to increase significantly due to the oxidation of $SiC_{(2-x)}$. Simultaneously, the peak intensity of $m/z = 30$ increases sharply. In the lower temperature regime, due to the uniform distribution of $SiC_{(2-x)}$ and BNC_x at the nano-scale in an amorphous structure, unoxidized $SiC_{(2-x)}$ inhibits the internal diffusion of oxygen and the further oxidation of BNC_x, and then in the higher temperature regime, oxidation of BNC_x is accelerated with synchronous oxidation of $SiC_{(2-x)}$ and BNC_x, which can be validated by transition of activation energy described in Section 2.3. In the high-temperature range (1000–1500 °C), Sample A-1 is further oxidized but the oxidation rate is much lower and increases slowly with temperature due to the change in the rate-limiting step. After oxidation in the middle-temperature range, the nanoparticulate structure of Sample A-1 is covered by a molten oxide layer with good fluidity. Due to the capillary forces, the powdered sample transforms into a monolithic sample composed of molten oxide and unoxidized amorphous ceramic. In consequence, the oxidation rate in the high-temperature regime is reduced due to the in-situ formation of a glassy oxide layer. Besides, due to more difficult gas diffusion in monolithic structures, the oxidation rate in the high-temperature stage is also controlled by gas diffusion in porous monoliths. Unlike the atomic diffusion in the oxide layer, the apparent activation energy of gas diffusion in pores is much lower, oxidation rate increases very slowly in this stage [27].

2.2.2. Effect of phase separation and structural evolution on the oxidation behaviors of crystalline SiBCN ceramics

The oxidation of SiBCN ceramics in the low and high-temperature ranges is determined by the oxidation of active sites on the surface and gas diffusion in the porous monoliths respectively, so the oxidation behavior of SiBCN ceramics is reflected only in middle temperature while crystalline C-1 and C-2 samples exhibit a different oxidation process in the middle-temperature range because phase separation in amorphous structure and structural evolution of crystalline structure result in a complex heterogeneous oxidation process. As shown in Fig. 4(b-c), the mass spectra of $m/z = 44$ (CO_2) and the DSC curves of the C-1 and C-2 samples show peak maxima in the lower temperature (550–850 °C) and higher temperature range (850–1200 °C). Besides, with increasing crystallization temperature, the peak intensity in $m/z = 44$ and DSC curves in the lower temperature range increases significantly with more obvious double peaked characteristics. Obviously, the double-peaked curves reflect the heterogeneous oxidation process and correspond to the oxidation process of two carbon-containing phases with different oxidation activities. According to the mass loss in the lower and mass gain in the higher temperature range, especially in Sample C-2, the peaks in the lower and higher temperature ranges are mainly caused by the oxidation of t-C and SiC respectively. Obviously, during phase separation, a larger number of carbon atoms bonded to both C and Si atoms existing inside the $SiC_{(2-x)}$ units or between the $SiC_{(2-x)}$ and BNC_x units in the amorphous SiBCN ceramics gradually disappear and transform to the combined carbon in the SiC phase and the free carbon in the t-C phase during crystallization with different oxidation activity, causing a heterogeneous oxidation characteristic of crystalline SiBCN ceramics and this effect will be magnified by structural evolution to nanocapsule-like structure. Specifically, in the microcrystalline structure, SiC and BN(C) crystallites are uniformly dispersed in the residual amorphous phase and in the BN(C) phase t-C layers are mutually stacked with t-BN layer. Thus, in the lower temperature range, the inert phase, especially the t-BN layer in the BN(C) phase, to a great extent inhibits the internal diffusion of oxygen and the oxidation of t-C in the BN(C) phase. However, in the nanocapsule-like structure, a loosely stacked BN(C) continuous phase is favorable to oxidation diffusion and much more vulnerable to oxidation, causing preferential oxidation of t-C in the lower temperature range.

The MS peak of $m/z = 30$ (NO) of the C-1 and C-2 samples shows a continuous single peak in the middle-temperature stage, indicating that t-BN undergoes continuous oxidation throughout the middle-temperature range. With the SiBCN ceramics transforming from an amorphous structure into a multi-phase structure, t-BN is more oxidized than SiC phase, especially in the nanocapsule-like structure, according to reduced intensities ratio between $m/z = 30$ and $m/z = 44$ spectra. Compared with t-BN phase in the crystalline structure, less oxidation of BNC_x in the amorphous structure is consistent with the formation of a dense N-containing amorphous oxide layer on the amorphous SiBCN monoliths as a passivating surface layer reported in Ref. [5]. In addition to the higher oxidation reactivity of t-BN, both, the phase distribution and the preferential oxidation of t-C at low temperatures also lead to enhanced oxidation of t-BN: Associated with the phase separation, well-crystallized SiC is encapsulated by loose turbostratic BN(C), so the continuous BN(C) phase becomes a favorable channel for oxygen diffusion and is preferentially oxidized. Besides, the consumed t-C layers at lower temperature promotes the diffusion of oxygen in BN(C) and the oxidation of the residual t-BN.

2.2.3. Different oxidation activities between amorphous and crystalline SiBCN ceramics

The peak temperature of the oxidation rate during non-isothermal oxidation is taken as a measure for the oxidation activities of the SiBCN ceramics. As shown in Fig. 4(e-f), the exothermic peak in the DSC curve is in good correspondence with the maxima of the mass change peaks in the DTG curves, reflecting the peak of oxidation rate during non-isothermal oxidation. The oxidation peak temperatures of the crystallized C-1 (1023 °C) and C-2 (1045 °C) samples are close to each other, but are much higher than that of amorphous Sample A-1 (873 °C), indicating that SiC and BN(C) phases have much lower oxidation activity than that of the $SiC_{(2-x)}$ and BNC_x in the amorphous state and require higher temperatures to achieve thermal activation. Besides, the temperature of the weight loss peak and the corresponding exothermic peak of Sample C-2 in the lower temperature range is around 760 °C, which is close to the peak temperature of the oxidation of graphite powder [28], which further indicates that the oxidation of free carbon occurs at this stage. However, the temperature corresponding to the exothermic peak in the lower temperature range of Sample C-1 is around 705 °C and lower than that of Sample C-2, due to lower degree of graphitization of BN(C) phase in microcrystalline structure than that in nanocapsule-like structure.

2.3. Structure and composition of oxide layer derived from amorphous and crystalline SiBCN ceramics

To analyze and evaluate the oxidation behavior and mechanisms of each SiBCN sample during the non-isothermal oxidation, the ceramics oxidized from room temperature to 1100 °C were prepared for characterization. The oxidation of all ceramics beyond 1100 °C is considered as the high-temperature oxidation regime. The oxidation process in the high-temperature range is controlled by the gas diffusion in porous monoliths and is related to the type and form of porosity of the porous monoliths which is beyond our research scope. As shown in Fig. 1(a), the XRD patterns of the three ceramics after oxidation show a diffuse peak at $2\theta = 22°$, corresponding to the amorphous borosilicate glass ($SiO_2{\cdot}xB_2O_3$) formed during oxidation (**Eq. (8)**). Except for the diffuse peak, Sample A-1 shows no further diffraction peaks, proofing no crystallization of Sample A-1 during oxidation. Diffraction peaks related to SiC in C-1 and C-2 samples after oxidation reveal almost no change in FWHM indicating no further crystallization during oxidation. However, the peak intensity decreased by 56.9% (Sample C-1) and 67.7% (Sample

C-2), respectively, since Sample C-2 compared to Sample C-1 is more severely oxidized. After oxidation, the weight gains of C-1 and C-2 samples are 17.9 wt% and 14.4 wt%, respectively. Theoretically, when SiBCN ceramics are completely transformed into oxide without volatilization of any oxide product, the weight gain is around 32.4 wt%. Thus, assuming homogeneous oxidation rather than heterogeneous oxidation, the oxidation ratio of C-1 and C-2 samples amount to 55.2 wt% and 44.4 wt% respectively, according to the mass change. For Sample C-1, the oxidation ratio calculated from the mass change (55.2 wt%) is close to that derived from XRD peaks (56.9%). However, for Sample C-2, the oxidation ratio calculated from the mass change (44.4 wt%) is much lower than that calculated from the XRD pattern (67.7%), mainly due to the preferred oxidation of the BN(C) phase. In particular, the preferential oxidation of t-C at lower temperatures already causes a significant weight loss (4.1 wt%) (see Fig. 4(c)). In fact, the actual oxidation ratio of Sample C-2 is even higher than 67.7% calculated from the XRD pattern of SiC phase, due to the less oxidation of SiC phase in Sample C-2. Due to the near homogeneous oxidation of Sample A-1, the oxidation ratio of amorphous Sample A-1 is inferred to be around 48.3% and much lower than the oxidation ratio of crystalline SiBCN ceramics especially the Sample C-2 with nanocapsule-like structure. Obviously, despite the much higher oxidation activity, the amorphous structure has an enhanced oxidation resistance than the crystalline structure, especially the nanocapsule-like structure because the oxidation resistance of SiBCN ceramics no longer depends exclusively on the oxidation activity of the individual atomic units or phases but also depends on the growth of oxide layer from the amorphous or multi-phase structure.

$$SiO_2(l) + xB_2O_3(l) \rightarrow SiO_2 \cdot xB_2O_3(l) \quad (8)$$

As shown in Fig. S7, the SiBCN ceramic powders consist of micron-sized aggregates stacked by many nanoparticles with a particle size of 50~200 nm. However, during oxidation, molten oxide glass heals the space between the closely packed nanoparticles in aggregates under the capillary force transforming the loosely stacked micron-sized aggregates to a porous monolith. To observe the microstructure inside the healed aggregates after oxidation, the porous monoliths were slightly ground into powder and observed by SEM. Fig. 5(a-c) shows the internal structure of different samples after oxidation: the oxidized aggregates are composed of molten oxides and unreacted core of a large number of nanoparticles. For Sample A-1, more obvious unreacted cores of nanoparticles are found inside the oxidized aggregates and the space inside aggregates is not completely healed by the oxide melt (see Fig. 5(a)). However, with crystallization in SiBCN ceramics, the aggregates are oxidized more severely with less unreacted core and residual pore inside oxidized aggregates (see Fig. 5(b-c)), indicating the presence of a higher fraction or better fluidity of molten oxides. Due to more difficult gas diffusion in healed aggregates of the crystalline SiBCN ceramics, the crystalline SiBCN ceramics show a lower oxidation rate in the high-temperature regime than the amorphous SiBCN ceramic (see Fig. 4) supporting the fact that the oxidation rate of the SiBCN ceramics in the high-temperature range is controlled by gas diffusion in the porous monolith. The EDS analysis results of the different spots in Fig. 5(a–c) are listed in Table 2, which reflect the change in the elemental composition of the SiBCN ceramics after oxidation. As shown in Table 2, after oxidation, the oxygen contents of the A-1, C-1 and C-2 samples increase to 42%, 46% and 58%, respectively, which is consistent with the more severe oxidation of crystalline SiBCN ceramic especially with nanocapsule-like structure. With crystallization, the residual carbon content of the oxidized ceramics decreases from 31.8% to 22.3%, due to the preferred oxidation of free carbon, especially in a nanocapsule-like structure.

Fig. S8 presents the deconvolution of XPS spectra of the different elements in the SiBCN ceramics after oxidation. Besides the fractions of the local bonding environment derived from the deconvolution of the XPS peaks are listed in Table 3, reflecting the composition of the oxide layer and heterogeneous oxidation process. As demonstrated in Fig. 1(b) and Fig. S8(b), due to preferential oxidation of the t-C phase especially in nanocapsule-like structure, after oxidation the content of C–C bonds of crystalline SiBCN ceramic (55.9%) is much lower than that in amorphous SiBCN ceramic (84.2%). Besides, the C-2 ceramic with a nanocapsule-like structure even exhibits a small amount of C–O bonds (10%). After oxidation, the peak intensity of O element increases significantly with a decrease in that of other elements, especially the N element (see Fig. 1(b-f)) and the Si–O and B–O bonds become the main valence bond form of Si and B (see Fig. 1(c-d)), so XPS spectra reflect the composition and valence bond environment of the oxide layer. Due to the preferential oxidation of t-BN than SiC phase in a nanocapsule-like structure, the ratio of B–O bonds to Si–O bonds (36%) in the oxidation product of Sample C-2 with nanocapsule-like structure is much higher than that of A-1 and C-1 samples (18–19%), so oxide layer of Sample C-2 has more B_2O_3 content in borosilicate glass with better fluidity. As shown in Fig. 1(f) and Fig. S4(f), the XPS peak of oxygen on the surface of different SiBCN ceramics presents a single peak with different degrees of asymmetry. The XPS peak of O in Sample A-1 has good symmetry because the O atoms exist in uniform borosilicate glass. However, the XPS peak of O element in the C-1 and C-2 samples shows a certain degree of asymmetry on the high binding energy side, reflecting the presence of B–O bonds of an incompletely dissolved B_2O_3. The content of the asymmetric part of Sample C-2 (15.3%) is higher than that of Sample C-1 (8.4%), demonstrating that compared with mixed SiC and BN(C) crystallites, the nanocapsule-like structure further inhibits B_2O_3 from effectively dissolving in SiO_2 to form a uniform borosilicate glass due to the growth of SiC grain and aggregation of the BN(C) phase.

Fig. 5(d-i) compares the oxide layer structure of crystalline SiBCN ceramic. As shown in Fig. 5(d), oxidized Sample C-1 presents a core-shell structure corresponding to the microstructure inside the healed aggregates and the oxide layer protects the unreacted core from oxidation. The SiC and BN(C) microcrystalline in the outer layer (Area 1) are completely consumed and converted into amorphous oxide while in the oxide layer near the unreacted core (Area 2), apart from a small amount of BN(C) phase, many residual SiC microcrystalline are dispersed in the

Table 2
EDS result of different spots in Fig. 5

EDS	Atomic content of element (%)				
	B	C	N	O	Si
Spot 1	9.5	31.8	3.3	42.9	12.5
Spot 2	9.4	28.7	3.7	46.3	11.9
Spot 3	7.5	22.3	2.0	55.0	13.2

Table 3
Quantification of local bonding environments of the post-oxidation samples of SiBCN ceramics based on deconvoluted XPS spectra.

Valence bond	A-1		C-1		C-2	
	BE (eV)	Content (%)	BE (eV)	Content (%)	BE (eV)	Content (%)
Si–C	101.0	6.8	101.0	8.6	100.5	4.1
Si–O	103.6	93.2	103.6	91.4	103.4	95.9
B–N	190.6	16.8	190.6	30.2	190.4	49.5
C–B–N	191.8	6.1	191.7	10.3	191.5	12.9
B–O	193.6	77.0	193.5	59.5	193.1	37.7
B–O–Si	533.2	100	533.1	91.6	532.8	84.7
O–B (B_2O_3)	–	–	534.5	8.4	534.2	15.3
C–Si	283.0	6.4	283.0	8.3	282.8	7.0
C–C	284.9	84.2	284.8	76.1	284.8	55.9
C–N	286.5	9.4	286.4	15.6	286.7	26.6
C–O	–	–	–	–	289.4	10.5
N–B (sp^2)	398.2	55.2	398.3	84.9	398.2	62.0
C–N–B	399.7	25.4	399.5	15.1	399.6	38.0
N–O	402.4	19.3	–	–	–	–

amorphous oxidation products (see Fig. 5(e-f)). Therefore, the oxidation of Sample C-1 is controlled to a certain extent by the diffusion of the oxide layer and the BN(C) phase is preferentially oxidized, becoming a channel for oxygen diffusion to promote the oxidation of residual SiC crystallites. In the process of continuous consumption of residual SiC, the oxidation product SiO_2 is continuously dissolved in the oxide layer to form a relatively uniform borosilicate glass, which can inhibit the volatilization of B_2O_3 and the crystallization of amorphous SiO_2. However, as shown in Fig. 5(g-i), Sample C-2 with a nanocapsule-like structure presents a different structure without obvious core-shell structure after oxidation: most of the BN(C) phase is consumed, the residual SiC grains with a size of about 30∼40 nm are dispersed in the amorphous oxidation products and the oxidation products contain many uniformly distributed amorphous dark spots with a size of about 3–5 nm indicating to the heterogeneity of oxide layer because nanocapsule-like structure further inhibits B_2O_3 from effectively dissolving in SiO_2 to form uniform borosilicate.

In summary, due to phase separation and structural evolution during crystallization, crystalline SiBCN ceramics especially those with a nanocapsule-like structure present a more obvious heterogeneous oxidation process and the oxide layer structure derived from the multi-phase structure, causing the degradation in the oxidation resistance. For one thing, the preferential consumption of BN(C) phase, especially the consumption of t-C in BN(C) phase at lower temperatures, provides a channel for oxygen diffusion and further promotes the oxidation of residual t-BN and SiC at higher temperatures and this effect will be magnified by a continuous distribution of BN(C) phase in nanocapsule-like structure. For another, unlike uniform distribution and the synchronous oxidation of the $SiC_{(2-x)}$ and BNC_x units in the amorphous structure, the preferential consumption of BN(C) phase, especially in nanocapsule-like structures, leads to excess B_2O_3 and heterogeneous composition in the oxide layer, which exacerbates the diffusion and volatility in the oxide layer. Specifically, due to the uniform distribution of $SiC_{(2-x)}$ and BNC_x at the nanometer scale, uniform borosilicate glass formed during oxidation has a lower oxygen diffusion coefficient and volatility than that of B_2O_3 and better liquidity than that of SiO_2. However, phase separation and structural evolution in crystalline SiBCN ceramics increase the diffusion distance of the oxidation product of BN(C) and SiC, so that B_2O_3 and SiO_2 cannot immediately form a uniform borosilicate glass. Therefore, the B_2O_3-rich zone volatilizes violently to form a large number of bubbles, and the SiO_2-rich zone with its relatively high viscosity cannot heal the formed defects. As a result, a loose porous oxide layer with poor protection against oxidation is formed (see supplementary material).

2.4. Oxidation kinetics of different atomic units or phases in amorphous and crystalline SiBCN ceramics

According to the analysis in Section 2.2, the oxidation process of the SiBCN ceramics strongly depends on the developed microstructure (amorphous versus polycrystalline). Besides, the MS peak of $m/z = 30$ represents the oxidation rate of the BNC_x units in the amorphous structure or that of the formed t-BN phase in the crystalline structure, while the MS peak of $m/z = 44$ is associated with the total oxidation rate of carbon-containing phases or units. After crystallization, the free carbon in t-C and the bonded carbon in SiC in the multi-phase microstructure of the C-1 and C-2 samples have different oxidation activities. Thus, two peaks in the $m/z = 44$ mass spectrum stand for the oxidation rates of t-C and SiC respectively. Although there is a proportional coefficient between the peak intensity of the mass spectrum and the oxidation rate, this proportional coefficient is incorporated into the constant parameters and does not affect the calculation of its kinetics. Therefore, according to the kinetic calculation method described in the supplementary material, the apparent activation energy (E_a) and rate-controlling mechanism of the different phases are obtained from the MS peaks of $m/z = 30$ and $m/z = 44$. According to the fitting results, the oxidation of each phase in all SiBCN ceramics conforms to the Zhuravlev-Lesokhin-Tempel (Z-L-T) equation of the D5 model. The D5 model as a kind of three-dimensional diffusion model is based on the assumptions of i) the presence of a solid reactant with a regular spherical shape, ii) the formation of a dense oxide layer and iii) a parabolic rate law of the oxide layer growth [29]. Therefore, the oxidation of the SiBCN ceramic is controlled by gas diffusion through the oxide layer and follows a parabolic rate law during the oxidation process like silicon-based ceramics such as SiC and Si_3N_4 [30].

Fig. 6 shows the fitting results of the oxidation kinetic curves of different phases or units in the ceramics. Although the initial and transition stages of the peaks will be disturbed by the background noise of the baseline and overlapping effect of peaks, with a large fitting deviation, it does not affect the kinetic analysis of the entire peak. In the middle-temperature range, the different atomic units or phases in SiBCN ceramic present different activation energy of oxidation, so the oxidation process is also controlled by the chemical reaction of the individual atomic unit or phase and the activation energy stands for their different oxidation activity in SiBCN ceramic. However, all oxidation kinetic curves of each atomic unit or phase in the ceramics are deflected in the high-temperature regime with much lower activation energy ($E_a < 90$ kJ/mol). In general, the gas diffusion rate is not sensitive to temperature compared to the rate of the chemical reaction and when the oxidation process is controlled by the diffusion of the gas, the apparent activation energy is less than 60–120 kJ/mol [27]. Therefore, the lower activation energy in the high-temperature regime further proves that the oxidation rate is controlled by the gas diffusion in the porous structure. The fitting effect of all kinetic curves in the high-temperature stage is poor (<96%) because their low peak intensity is superimposed by the background noise of the baseline. The activation energy of the amorphous Sample A-1 in the high-temperature range ($E_a = 143$ kJ/mol) is significantly higher than that of crystalline C-1 ($E_a = 57$–59 kJ/mol) and C-2 ($E_a = 61$–82 kJ/mol) samples, which is consistent with the analysis in Section 2.2. Due to less oxidation and higher viscosity of the oxide layer, in oxidized Sample A-1, the space inside aggregates is not completely healed by the oxide melt with a loose structure enhancing the gas diffusion in porous monolith (see Fig. 5(a)). Therefore, the oxidation rate of Sample A-1 at high temperatures is also controlled by oxide layer diffusion or oxidation reaction to a certain degree, rather than completely controlled by gas diffusion, resulting in higher activation energy than that of the general gas diffusion ($E_a <$ 60–120 kJ/mol).

Fig. 6(a) shows the fitting results of the oxidation kinetic curves of carbon-containing units in the amorphous structure and the SiC phase in the crystalline structure. It is found that the oxidation kinetic curves of C-1 and C-2 samples in the middle-temperature stage show a good fitting effect ($R^2 > 99.4\%$), while the fitting effect of Sample A-1 is relatively poor ($R^2 = 96.1\%$). For Sample A-1, the total apparent activation energy in the middle-temperature stage (550–1050 °C) is about 218 kJ/mol, but the kinetic curve is significantly deflected at 750 °C, causing a poor fitting effect. Therefore, the kinetic curve is well fitted in the two temperature regimes dividually ($R^2 > 99.7\%$) to obtain the activation energies at 550–750 °C and 750–1050 °C, respectively (see Fig. S9). The activation energy at 750–1050 °C ($E_a = 332$ kJ/mol) is much higher than that 550–750 °C ($E_a = 145$ kJ/mol), which verifies the analysis in Section 2.2.1: the oxidation kinetic curve at 550–750 °C reflects the oxidation of carbon in BNC_x with a lower oxidation activation energy while that at 750–1050 °C more reflects the oxidation of C atoms in the $SiC_{(2-x)}$ units with a higher oxidation activation energy.

Fig. 6(b) shows the fitting result of the oxidation kinetic curves of BNC_x or t-BN in the different ceramics. Due to the weak intensity of the $m/z = 30$ peak of Sample A-1, its intensity in the high-temperature stage is greatly affected by the background noise of the baseline, so only its oxidation kinetic curve in the middle-temperature stage is calculated, exclusively. As shown in Fig. 6(b), the oxidation kinetic curve of the N element in Sample A-1 deflects obviously at around 830 °C and by fitting in different stages, it is obtained that the oxidation activation energy

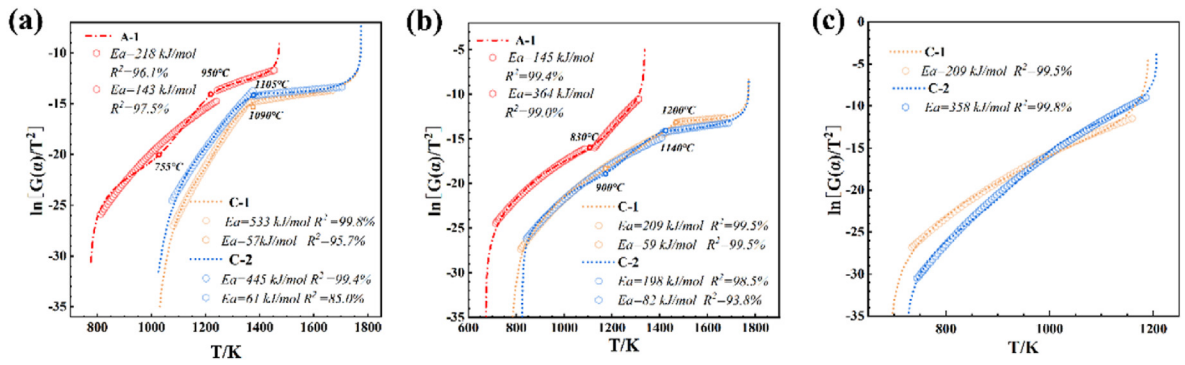

Fig. 6. Kinetic calculation of different components in SiBCN ceramics: (a) SiC; (b) BN; (c) C.

above 830 °C (E_a = 364 kJ/mol) is significantly higher than that below 830 °C (E_a = 145 kJ/mol). In addition, above 830 °C, in Sample A-1, the oxidation activation energy of the N element (E_a = 145 kJ/mol) is almost equal to that of the C element (E_a = 145 kJ/mol) (see Fig. S9 and Fig. 6(b)), further indicating oxidation of BNC_x units in amorphous structure in the lower-temperature range. However, above 830 °C, the synchronous oxidation of the $SiC_{(2-x)}$ and BNC_x units changes the oxidation activation energy of BNC_x to that similar to $SiC_{(2-x)}$ (E_a = 332 kJ/mol). By careful observation, it is found that the oxidation kinetic curves of t-BN in C-1 and C-2 samples also have a slight deflection at about 900 °C. In the lower-temperature stage, B_2O_3 as the main oxidation product has a high oxygen diffusion coefficient with lower diffusion activation energy, while with oxidation of SiC phase in the higher temperature range, SiO_2 continuously dissolves in B_2O_3 to form a borosilicate glass, increasing diffusion activation energy of the oxide layer and a slight deflection above 900 °C. However, due to the multi-phase structure and heterogeneous oxidation process, in crystalline SiBCN ceramics, t-BN phase has a much lower activation energy SiC phase, unlike the similar oxidation activation energy of BNC_x and $SiC_{(2-x)}$ during synchronous oxidation.

Due to the extremely higher oxidation activity of amorphous structure, $SiC_{(2-x)}$ atomic unit (E_a = 364 kJ/mol) in amorphous Sample A-1 presents much lower activation energy than that of the SiC phase in crystalline C-1 (E_a = 533 kJ/mol) and C-2 (E_a = 445 kJ/mol) samples and the BNC_x (E_a = 145 kJ/mol) has much lower activation energy than the t-BN phase in C-1 (E_a = 209 kJ/mol) and C-2 (E_a = 198 kJ/mol) samples. However, despite of higher oxidation activity of SiC and t-BN phase in Sample C-2 than in Sample C-1 due to graphitization of t-BN and growth of SiC grain, the oxidation activation energy (E_a = 198 kJ/mol, E_a = 445 kJ/mol) of SiC and t-BN phases in C-2 sample is slightly lower than that in C-1 sample (E_a = 209 kJ/mol, E_a = 533 kJ/mol) because the apparent activation energy of SiC and t-BN phases is also determined by the diffusion through the formed oxide layer. The oxide layer of Sample C-2 is rich in B_2O_3 that is not dissolved in the borosilicate glass, which promotes diffusion in the oxide layer with the consequence of a decrease in the diffusion activation energy of the oxide layer. Fig. 6(c) shows the fitting results of the oxidation kinetic curves of t-C in the crystalline C-1 and C-2 samples (R^2 > 99.5%): The oxidation of t-C is not influenced by the diffusion of oxide layer due to the preferential oxidation of t-C at low temperatures, so unlike the SiC and t-BN phase, the activation energy of t-C in Sample C-2 (E_a = 358 kJ/mol) is much higher than that of Sample C-1 (E_a = 209 kJ/mol), due to higher degree of graphitization of t-C in Sample C-2.

3. Conclusions

In this study, the structural evolution during the crystallization of amorphous SiBCN ceramics and its effect on the oxidation behavior and kinetics of different atomic units or phases in the amorphous and crystalline SiBCN ceramics were investigated in detail. The main results are as follows.

(1) During crystallization, the SiBCN ceramics transform from an amorphous structure composed of $SiC_{(2-x)}$ (x < 1) and BNC_x atomic units (Sample A-1) to a microcrystalline structure with precipitated SiC and BN(C) microcrystalline (2–5 nm) (Sample C-1), and then to a nanocapsule-like structure (20–50 nm) by twisting and merging of adjacent SiC crystallites and aggregation of the BN(C) phase (Sample C-2).

(2) The amorphous structure has exceptionally high oxidation activity but presents much better oxidation resistance due to its synchronous oxidation of atomic units and homogeneous composition in the generated oxide layer. However, during crystallization, a larger number of carbon atoms bonded to both C and Si atoms exist inside the $SiC_{(2-x)}$ units or between the $SiC_{(2-x)}$ and BNC_x units in the amorphous SiBCN ceramics, transforming to the combined carbon in the SiC phase and the free carbon mainly in the t-C phase during crystallization, and the phase separation degrades the oxidation resistance of SiBCN ceramic especially that with nanocapsule-like structure, because the preferential consumption of BN(C) phase, especially the t-C in BN(C) phase, provides a channel for oxygen diffusion and this effect will be magnified by a continuous distribution of BN(C) phase in nanocapsule-like structure.

(3) Compared with crystalline ceramics, amorphous SiBCN ceramics present enormously high oxidation activity and can be severely oxidized even at room temperature to form fine oxide particles containing Si–O, B–O and N–O bonds on their surface. Therefore, BNC_x (E_a = 145 kJ/mol) and $SiC_{(2-x)}$ (E_a = 364 kJ/mol) atomic units in amorphous SiBCN structure (Sample A-1) can be oxidized at relatively lower temperatures with much lower activation energy than the corresponding BN(C) (E_a = 209 kJ/mol) and SiC (E_a = 533 kJ/mol) phases in crystalline structure (Sample C-1) and the synchronous oxidation of the $SiC_{(2-x)}$ and BNC_x units above 750 °C changes the oxidation activation energy of BNC_x (E_a = 332 kJ/mol) to that similar to $SiC_{(2-x)}$.

(4) The aggregation of the BN(C) phase and preferential consumption of BN(C) phase in nanocapsule-like structure lead to excess B_2O_3 and heterogeneous composition in the oxide layer, decreasing the apparent activation energy of SiC (Ea = 445 kJ/mol) and t-BN (Ea = 198 kJ/mol) in Sample C-2.

4. Materials and method

4.1. Powder preparation

The raw materials of cubic silicon (c-Si) powder (Beijing Mengtai Research and Development Center Co., Ltd., Beijing), hexagonal boron nitride (h-BN) powder (Fangyuan Boron Nitride Factory Co., Ltd., China), and graphite powder (Qingdao Huatai Lubrication and Sealing Technology Co., Ltd., China) with the atomic ratio of Si:C:B:N = 2:3:1:1 were mechanically alloyed by high-energy ball milling for 40 h to prepare

amorphous SiBCN ceramic nanopowder with a particle size of 50~200 nm as amorphous Sample A-1. To observe the structural evolution during crystallization, the amorphous SiBCN nanopowder (A-1) was held for an hour at 1600 °C and 1900 °C in a nitrogen atmosphere at atmospheric pressure and the resulting materials are denoted as Sample C-1 and C-2, respectively. The samples of A-1, C-1, and C-2 have a similar specific surface of 22~25 m^2/g, due to their same particle size, which is necessary for comparison for oxidation of amorphous and crystalline SiBCN ceramics.

4.2. Non-isothermal oxidation experiment

Non-isothermal oxidation test of the SiBCN nano-powders was conducted on a simultaneous thermal analyzer-mass spectrometer (STA449F3, Netzsch Group, Germany) and the TG curve, DSC curve, and MS spectra of the gas products were recorded synchronously. The samples were heated to 1500 °C at a rate of 10 °C/min in a simulated air atmosphere (O_2: Ar = 1: 4) with a total gas flow of 100 mL/min. The test was repeated three times for each sample to ensure the accuracy and repeatability of the experiment. To analyze the microstructure of the oxidized powders after being heated to 1100 °C in the above non-isothermal oxidation test, the powders in the crucibles were placed in a muffle furnace, heated to 1100 °C at a rate of 10 °C/min in air, and then taken away from the furnace quickly.

4.3. Characterizations

The morphology of the amorphous and crystallized SiBCN ceramic powders before and after oxidation was observed by scanning electron microscopy (SEM, SU5000, Hitachi Co., Japan). The microstructure and elemental distribution of the different SiBCN ceramics before and after oxidation were analyzed by transmission electron microscope (TEM, JEM-F200, JEOL Ltd., Japan; Talos F200X, FEI, USA) with selective area electron diffraction (SAED), high-resolution transmission electron imaging (HRTEM) and energy dispersive spectrometry (EDS). The phase composition of the different SiBCN ceramics before and after oxidation was characterized by X-ray diffractometer (XRD, X'PERT, Panalytical Instruments Co., Netherlands) with a scanning range of $2\theta = 10–90°$ and a scanning speed of 4°/min. The atom bonding state on the surface of the SiBCN ceramics before and after oxidation was characterized by an X-ray photoelectron spectrometer (XPS, ESCALAB 250Xi, ThermoFisher Co., USA). Structural information of the formed carbon phase in the SiBCN ceramics was characterized by Raman spectroscopy (Raman, inVia, Renishaw Co., UK). The oxygen content of the amorphous and crystallized SiBCN ceramic powders was determined by an oxygen-nitrogen-hydrogen analyzer (ONH836, LECO Co., USA). The specific surface area of the powder was studied through nitrogen adsorption at 77K by a physical chemistry adsorption instrument (ASAP 2020, Micromeritics Instrument Corp, USA).

Author contribution

Zi-bo Niu: conceptualization, methodology, investigation, formal analysis, writing—original draft; Daxin Li: conceptualization, methodology, supervision; Dechang Jia: conceptualization, methodology, supervision; Zhihua Yang: manuscript revision, supervision; Kunpeng Lin: Data curation, formal analysis; Paolo Colombo: manuscript revision; Ralf Riedel: manuscript revision; Yu Zhou: manuscript revision; All authors have given approval to the final version of the manuscript.

Data availability

All data needed to evaluate the conclusions in the paper are present in the paper and the Supplementary Materials.

Declaration of competing interests

Prof. Ralf Riedel is an editorial board member for Advanced Powder Materials and was not involved in the editorial review or the decision to publish this article. All authors declare that there are no competing interests.

Acknowledgements

This work was financially supported by the National Natural Science Foundation of China (Grant no. 52002092, 51832002, 52172068, 52232004, 52372059), Heilong Jiang Natural Science Fund for Young Scholars (Grant no. YQ2021E017), National Key Research and Development Program of China (Grant no. 2017YFB0310400), Heilongjiang Touyan Team Program, Advanced Talents Scientific Research Foundation of Shenzhen, and Fundamental Research Funds for the Central Universities (2022FRFK0600XX). RR gratefully acknowledges the financial support provided by the Research Training Group 2561 "MatCom-ComMat: Materials Compounds from Composite Materials for Applications in Extreme Conditions" funded by the Deutsche Forschungsgemeinschaft (DFG), Bonn, Germany.

Appendix A. Supplementary data

Supplementary data to this article can be found online at https://doi.org/10.1016/j.apmate.2023.100163.

References

[1] R. Riedel, A. Kienzle, W. Dressler, L. Ruwisch, J. Bill, F. Aldinger, A silicoboron carbonitride ceramic stable to 2000°C, Nature 382 (6594) (1996) 796–798.
[2] D. Jia, B. Liang, Z. Yang, Y. Zhou, Metastable Si–B–C–N ceramics and their matrix composites developed by inorganic route based on mechanical alloying: Fabrication, microstructures, properties and their relevant basic scientific issues, Prog. Mater. Sci. 98 (2018) 1–67.
[3] A. Müller, P. Gerstel, M. Weinmann, J. Bill, F. Aldinger, Correlation of boron content and high temperature stability in Si–B–C–N ceramics, J. Eur. Ceram. Soc. 20 (14–15) (2000) 2655–2659.
[4] X. Ji, S. Wang, C. Shao, H. Wang, High-temperature corrosion behavior of SiBCN fibers for aerospace applications, ACS Appl. Mater. Interfaces 10 (23) (2018) 19712–19720.
[5] B. Liang, Z. Yang, D. Jia, J. Rao, D. Yu, Y. Tian, Q. Li, Y. Miao, Q. Zhu, Y. Zhou, Amorphous silicoboron carbonitride monoliths resistant to flowing air up to 1800 °C, Corrosion Sci. 109 (2016) 162–173.
[6] D. Li, Z. Yang, D. Jia, X. Duan, D. Cai, P. He, S. Wang, Y. Zhou, Dense amorphous $Si_2BC_{1-4}N$ monoliths resistant to high-temperature oxidation for hypersonic vehicle, Corrosion Sci. 163 (2020) 108231.
[7] D. Li, D. Jia, Z. Yang, Y. Zhou, Principles, design, structure and properties of ceramics for microwave absorption or transmission at high-temperatures, Int. Mater. Rev. 67 (3) (2022) 266–297.
[8] X. Yin, L. Kong, L. Zhang, L. Cheng, N. Travitzky, P. Greil, Electromagnetic properties of Si–C–N based ceramics and composites, Int. Mater. Rev. 59 (2014) 326–355.
[9] A.M. Hermann, Y. Wang, P.A. Ramakrishnan, D. Balzar, L. An, C. Haluschka, R. Riedel, Structure and electronic transport properties of Si–(B)–C–N ceramics, J. Am. Ceram. Soc. 84 (2001) 2260–2264.
[10] A. Xia, B. Zhang, J. Yin, X. Chen, S. Lee, X. Liu, Z. Huang, Cross-scale microstructure design of precursor-derived SiC-AlN nanoceramic composites hybrid with ex-situ ZrB_2, Adv. Powder Mater. 2 (1) (2023) 100063.
[11] J.A. Golczewski, F. Aldinger, Phase separation in Si–(B)–C–N polymer-derived ceramics, Int. J. Mater. Res. 97 (2022) 114–118.
[12] J. Haug, P. Lamparter, M. Weinmann, F. Aldinger, Diffraction study on the atomic structure and phase separation of amorphous ceramics in the Si−(B)−C−N system. 2. Si−B−C−N ceramics, Chem. Mater. 16 (2004) 83–92.
[13] M. Zhang, D. Li, Y. Hong, Z. Niu, Z. Yang, D. Jia, Y. Zhou, Study on the oxygen diffusion in the oxide layers of SiBCN ceramics by SIMS, J. Eur. Ceram. Soc. 42 (4) (2022) 1341–1347.
[14] M. Zhang, Q. Chen, Y. Peng, Y. Hong, D. Li, Z. Yang, D. Jia, D. Cai, Z. Niu, J. Guan, B. Wang, A comparative study on high temperature oxidation behavior of SiC, SiC-BN and SiBCN monoliths, Corrosion Sci. 192 (2021) 109855.
[15] M.K. Cinibulk, T.A. Parthasarathy, Characterization of oxidized polymer-derived SiBCN fibers, J. Am. Ceram. Soc. 84 (10) (2001) 2197–2202.
[16] E. Butchereit, K.G. Nickel, A. Müller, Precursor-derived Si–B–C–N ceramics: Oxidation kinetics, J. Am. Ceram. Soc. 84 (10) (2001) 2184–2188.
[17] Z. Yu, F. Li, Q. Zhu, Single-source-precursor synthesis and phase evolution of NbC-SiC-C ceramic nanocomposites with core shell structured NbC@C and SiC@C nanoparticles, Adv. Powder Mater. 1 (1) (2022) 100009.

[18] X. Huang, L. Bao, R. Bao, L. Liu, J. Tao, J. Wang, Z. Zhang, Z. Ge, S. Tan, J. Yi, F. Meng, Reinforced copper matrix composites with highly dispersed nano size TiC in-situ generated from the Carbon Polymer Dots, Adv. Powder Mater. 2 (2) (2023) 100090.
[19] P. Zhang, D. Jia, Z. Yang, X. Duan, Y. Zhou, Microstructural features and properties of the nano-crystalline SiC/BN(C) composite ceramic prepared from the mechanically alloyed SiBCN powder, J. Alloys Compd. 537 (2012) 346–356.
[20] Y. Zhan, W. Li, T. Jiang, C. Fasel, E. Ricohermoso, J. Bernauer, Z. Yu, Z. Wu, F. Müller-Plathe, L. Molina-Luna, R. Grottenmüller, R. Riedel, Boron-modified perhydropolysilazane towards facile synthesis of amorphous SiBN ceramic with excellent thermal stability, J. Adv. Ceram. 11 (2022) 1104–1116.
[21] Z. Yang, D. Chang, Y. Zhou, Silicon-boron-carbon-nitrogen System Metastable Ceramics and its Composite Materials Prepared by Inorganic Method, Science Press, Beijing, 2019.
[22] B. Wang, D. Li, Z. Yang, D. Jia, J. Guan, D. Cai, P. He, X. Duan, Y. Zhou, Study on oxidation resistance and oxidative damage mechanism of SiBCN-Ta_4HfC_5 composite ceramics, Corrosion Sci. 197 (2022) 110049.
[23] R. Riedel, L.M. Ruswisch, L. An, R. Raj, Amorphous silicoboron carbonitride ceramic with very high viscosity at temperatures above 1500 °C, J. Am. Ceram. Soc. 81 (12) (2010) 3341–3344.
[24] A. Oberlin, Pyrocarbon, Carbon 40 (4) (2002) 7–24.
[25] P. Lespade, A. Marchand, M. Couzi, F. Cruege, Caracterisation de materiaux carbones par microspectrometrie Raman, Carbon 22 (4–5) (1984) 375–385.
[26] P. Atkins, P.W. Atkins, J. Paula, Atkins' Physical Chemistry, Oxford university press, New York, 2014.
[27] W.W. Porterfield, Inorganic Chemistry, Academic Press, New York, 2013.
[28] H. Badenhorst, B. Rand, W.W. Focke, Modeling of natural graphite oxidation using thermal analysis techniques, J. Therm. Anal. Calorim. 99 (2010) 211–228.
[29] A.K. Tripathy, P.K. Pattnayak, H.S. Ray, Modification of Jander's equation for kinetic analysis of data on a solid state reaction, in: Proceedings of the Seminar on Experimental Approaches in Pyrometallurgical Research, Allied Publishers, 2000.
[30] K.L. Luthra, Some new perspectives on oxidation of silicon carbide and silicon nitride, J. Am. Ceram. Soc. 74 (5) (1991) 1095–1103.

Zi-bo Niu is a Ph. D. candidate in Institute of Advanced Ceramics in the Materials Science and Engineering Department, Harbin Institute of Technology. He received his M.S. in Powder Metallurgy Research Institute from Central South University in 2020. His research focuses on the Ceramic matrix composites and precursor derived ceramics and nanocrystalline ceramics (E-mail: ziboniu1236@163.com).

Currently, **Dr. Daxin Li** works at Harbin Institute of Technology as an associate professor/master tutor. He got his Ph.D. degree from Harbin Institute of Technology in 2018 and was selected for the 2019 Postdoctoral Innovative Talent Support Program. His research focuses on the structural evolution and damage mechanisms of SiBCN-based metastable ceramics and their composites under severe service environments such as high temperature, severe thermal shock, and strong ablation. He has more than 30 peer-reviewed journal papers published/accepted, four granted patents, and one book.

Currently, **Prof. Dechang Jia** works at Harbin Institute of Technology as director of the Institute for Advanced Ceramics (http://iac.hit.edu.cn) and the Key Laboratory of Advanced Structural-Functional Integration Materials & Green Manufacturing Technology (http://mgmt.hit.edu.cn). He is mainly engaged in scientific research and teaching work on advanced ceramics, ceramic matrix composites, and their applications in extremely harsh service environments. He was funded by the National Fund for Distinguished Young Scholars in 2012 and was selected as Youth Science and technology innovation leader, and leading Talent of "Ten Thousand Plan". He won the second prize of national award for technological invention, got 60 granted patents, and has published 360 co-published papers in SCI, 320 papers in EI, and 8 monographs.